Liquid Crystals
Publication details, including instructions for authors and subscription information:
http://www.informaworld.com/smpp/title~content=t713926090

Computational modelling of light propagation in textured liquid crystals based on the finite-difference time-domain (FDTD) method

Dae Kun Hwang[a]; Alejandro D. Rey[a]
[a] Department of Chemical Engineering, McGill University, Montreal, Quebec, Canada H3A 2B2

To cite this Article Hwang, Dae Kun and Rey, Alejandro D.(2005) 'Computational modelling of light propagation in textured liquid crystals based on the finite-difference time-domain (FDTD) method', Liquid Crystals, 32: 4, 483 — 497
To link to this Article: DOI: 10.1080/02678290500033950
URL: http://dx.doi.org/10.1080/02678290500033950

Liquid Crystals, Vol. 32, No. 4, April 2005, 483–497

Taylor & Francis
Taylor & Francis Group

Computational modelling of light propagation in textured liquid crystals based on the finite-difference time-domain (FDTD) method

DAE KUN HWANG and ALEJANDRO D. REY*
Department of Chemical Engineering, McGill University, 3610 University Street, Montreal, Quebec, Canada H3A 2B2

(*Received 13 May 2004; accepted 18 October 2004*)

Light propagation through uniaxial rod-like nematic liquid crystal films containing singular (thin) and non-singular (thick) line disclinations is computed using the finite-difference time-domain method (FDTD), which is based on accurate numerical solutions to the governing Maxwell equations. The results obtained by the FDTD method are compared with classical matrix-type methods, including the aggregate model and Berreman's method. It is found that the optical signals for singular and non-singular defects predicted by the matrix methods deviate significantly from the FDTD method because director gradient effects on the plane normal to the incident light are not properly taken into account . It is also found that the FDTD optical signal for singular thin lines has a characteristic length scale associated with the wavelength of the incident light, while for non-singular thick lines the scale is associated with the defect escaped core dimensions. The FDTD method offers an accurate quantitative tool for use in new applications including liquid crystal-based biosensors and rheo-optical characterization of liquid crystalline polymers.

1. Introduction

The optical properties of low molar mass liquid crystals (LCs) form the basis of most of their applications in display devices [1]. Properly designed substrates (surface fields) are highly efficient in aligning and producing defect-free nematic liquid crystal (NLC) films. The application of this ability has spawned the entire liquid crystal display (LCD) industry. As a consequence, research in the surface science of liquid crystals has received the most attention and resources in this field. Since the proper functioning of most LCDs relies on the formation of defect-free layers, physicochemical surface treatments of many different substrates have been developed. In general, isotropic untreated surfaces, such as glass, give rise to defect textures due to the lack of a unique and sufficiently strong orienting surface field. The ability optically to detect the transformation of the surface field of a substrate by physicochemical processes can be the basis of signal generation in a sensor device. Placing a NLC film between two substrates produces a texture whose optical response to linearly polarized light, when viewed between crossed polarizers, is unique and quantifiable; thus the key characteristics (i.e. surface topology, surface charge, chemical composition, heterogeneity) of any physiochemical surface process that creates textural changes in NLC films is detectable and quantifiable. Abbott and Skaife have developed a new biosensor device that quantitatively detects the presence of complex biomolecules based on the optical response of liquid crystal films deposited on nano-structured substrates [2, 3]. This device shows many potential advantages over currently used biosensor devices in terms of the response time, simplicity and expense. The device also shows high capabilities of selectivity, sensitivity and accuracy, which are critical factors for biosensors. The device is based on surface-induced texture generation in thin NLC films formed between protein-coated substrates. In the absence of protein coating, the nano-strucured substrates induce defect-free NLC monodomains, while substrates with adsorbed protein produce characteristic NLC textures. By measuring the intensity of transmitted optical polarized light when placing the film between crossed polarizers, a quantitative relation between the optical signal and the amount of adsorbed protein is established. In spite of the successful quantifications based on the optical signals of the LC textures induced by the bounding events of the biomolecules on the substrates, the relationships between the surface-induced LC textures and the bounding events of the biomolecules on the surface are not fully understood.

The characterization of thermotropic and lyotropic liquid crystal polymers (LCPs) used in the production of fibres and films, is based on rheo-optical measurements

*Corresponding author. Email: alejandro.rey@mcgill.ca

Liquid Crystals
ISSN 0267-8292 print/ISSN 1366-5855 online © 2005 Taylor & Francis Group Ltd
http://www.tandf.co.uk/journals
DOI: 10.1080/02678290500033950

[4]. Flow-induced textural transformations are associated with certain viscosity reduction mechanisms as the shear rate increases. The underlying director field and defect distribution that defines the texture is imprinted on the optical signal when viewing the flowing polymer under crossed polarizers, but at present the relation between optcal signal and textural details remains poorly understood, basically due to lack of computational modelling studies. These two examples show the great need for computational modelling of light propagation in heterogeneous and textured LCs for quantitative characterization of surface- and flow-driven texturing processes.

Many optical methods for light propagation through LCs cells have been proposed in order to determine optical properties of the LCs and improve devices based on LC optics. Since the first introduction of the Jones 2×2 matrix method [5], matrix-type methods based on the stratified-medium approach have been widely used for optical simulation of LC optics due to its simplicity. The main application of matrix-type methods has been in LC display devices. However, multiple reflections due to the existence of different media are neglected in the Jones 2×2 matrix method which is also restricted only to the normal incidence case. To overcome the limitations, Berreman introduced the 4×4 matrix method accounting for multiple reflections and oblique incidence cases [6]. Later, extensions of the Jones matrix method were formulated to overcome multiple reflections [7], and oblique incidence cases [8]. In spite of these improvements, another major restriction remains in the matrix-type methods due to the assumption that the variation of the dielectric tensor occurs only along the direction of wave propagation [5–7]. In the matrix-type methods, a computational domain is divided into a finite number of layers and the dielectric tensor is assumed to be uniform in each layer. The accuracy of the methods therefore depends on the size of the layer. These methods are still valuable for LC display device applications when each individual pixel exceeds the extent of many optical wavelengths and there is a slow variation of LC orientation along the transverse directions [9]. Consequently, most applications of the matrix-type methods are one-dimensional problems in which the only allowed spatial variation is along the normal to the LC displays [8, 10–12]. However, a significant number of currently evolving LC display devices such as small-sized pixels for head-mounted displays, pixel edges, and multi-domain LC displays in which the pixel size becomes very small, the homogeneity along the pixel reduces, and domains with different director orientations can occur [13, 14]. In addition to the advanced display devices, biosensor applications on NLCs and rheo-optical characterization of LCPs all require computational modelling using optical methods that resolve multi-dimensional and multi-scale spatial heterogeneities.

Small molar mass NLC textures, containing point and lines defects, were simulated by Nicholson using the aggregate model, which is similar to the Jones matrix method [15]. In this method a three-dimensional computation domain is divided into finite cubic lattices of uniform dielectric permitivity tensor. A similar approach is used for simulation of textures in LC droplets [16]. This approach may not be qualitatively rigorous for optical simulation of the LC defects, since there is strong variation of the director field over small length scales in more than one dimension. Analysis textures in biosensors and rheo-optical devices, containing small scale multi-dimensional heterogeneities in the director field require refined and rigorous numerical methods for electromagnetic propagation.

The finite-difference time-domain (FDTD) method is a rigorous numerical method used to solve Maxwell's curl equations and is an efficient tool for simulation of light propagation in LCs containing complex textures. Since the first introduction of the FDTD method by Yee [17], it has been implemented in an electromagnetic field such as light propagation, scattering, guiding, and inverse scattering in arbitrary structures and in homogeneous or anisotropic materials [18]. The major improvement of the FDTD method in terms of accuracy and efficiency came after Berenger [19] proposed the perfectly matched layer (PML) instead of the conventional Mur [20] absorbing boundary for efficient truncation of computational domains. Despite widespread use of the FDTD method, its application to LC optics has only recently been introduced. Two-dimensional wave propagation in a twisted nematic display was determined using the FDTD method [21], and its accuracy was assessed against the analytical solution in the one-dimensional twisted nematic structure [22]. More advanced work on two-dimensional wave propagation in a LC display containing bend/splay and titled/twisted deformations in LC devices, and domain-walls in ferroelectric LC devices [13, 14, 23] have been conducted. The application of the FDTD method was recently expanded to 3D wave propagation in LC devices [24]; even though, its use for simulation of LC optics has been successfully proven, it has not been fully explored in LC films containing various types of defects such as those observed in Abbot's biosensor device and in rheo-optical devices.

The objective of this paper is to determine wave propagation in uniaxial nematic LCs containing simple defects using the FDTD method. The results

obtained are compared with matrix-type methods, including the aggregate model and the Berreman method. For the purpose of comparison with the aggregate model results [15], only the normal incident case is considered in our study. Having established the accuracy and resolution of the LC FDTD method for single defects, later work will report on LC optics of high density textures.

2. Light transmission models

In this section we present the three basic light transmission models used to compute the optical response of uniaxial NLC films: (i) the aggregate model [15, 16, 25], (ii) the Berreman method [11, 26, 27] and (iii) the FDTD method [28]. The actual computational process (i.e. matrix computations, evaluations of discrete calculus terms, etc.) for each method is given in § 3. In the three cases we consider a NLC thin film placed between crossed polarizers, and only the main equations and procedures are discussed in detail. The average molecular orientation is defined by the unit vector **n** known as the director, or optic axis.

2.1. *The aggregate model*

The computational space for the NLC film is divided into a set of uniaxial finite cubic lattices, of a uniform dielectric constant [15, 16]. The computational space in the aggregate model is illustrated in figure 1. The propagation direction is the z direction. The optic axis is only a function of z: $\mathbf{n}=\mathbf{n}(z)$.

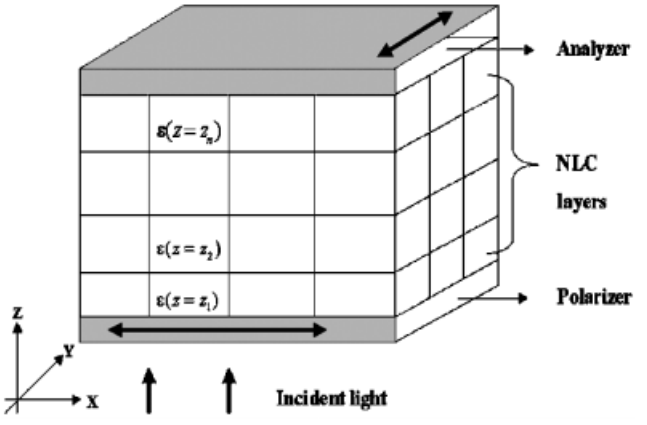

Figure 1. Schematic diagram of the computational domain between crossed polarizers for the aggregate model, definition of rectangular coordinate system, and direction of incident light. In this model there are no glass substrates bounding the nematic liquid crystal (NLC).

Monochromatic incident light, which has a complex time dependency $E=E_o\exp(\mathrm{i}\omega t)$, is introduced to the computational space, where E_o is the magnitude and ω is the angular frequency. The known tangential components of the polarized light $E_{x\mathrm{p}}$ and $E_{y\mathrm{p}}$ after the incident light $E=E_o\exp(\mathrm{i}\omega t)$ passes through the ideal polarizer which is parallel to the x direction is computed using:

$$\begin{bmatrix} E_{x\mathrm{p}} \\ E_{y\mathrm{p}} \end{bmatrix} = \begin{bmatrix} \sin\theta_{\mathrm{p}} \\ \cos\theta_{\mathrm{p}} \end{bmatrix} E_{\mathrm{o}} \exp(\mathrm{i}\omega t) \tag{1}$$

where θ_{p} is the direction of the polarizer with respect to the x direction. The polarized incident light propagates through the cubic cells in two mutually orthogonal directions; the direction parallel to the optic axis is called the extraordinary ray and the direction perpendicular to the optic axis is called the ordinary ray. Due to the variation of the optic axis and the birefringence of the NLC film, the polarized light experiences rotation and phase shift within the NLC film. The emerging light from the first cubic cell in a column, after taking into account the rotation and retardation, is computed as follows:

$$\begin{bmatrix} E_{x1} \\ E_{y1} \end{bmatrix} = \begin{bmatrix} E_{\mathrm{o}} \cos\phi_1 \exp(\mathrm{i}\omega t)\exp(-\mathrm{i}\delta_1) \\ E_{\mathrm{o}} \sin\phi_1 \exp(\mathrm{i}\omega t) \end{bmatrix} \tag{2}$$

where δ_1 is the phase retardation due to the tilt angle of the optical axis with respect to the xy plane, ϕ_1 is the azimuthal angle of the optic axis with respect to the x direction, and the subscript 1 indicates the first cubic cell in the column. Further rotation and phase lag of the light emerging from the first lattice cell occurs within the second cell. The emergent light from the second cell is given by

$$\begin{bmatrix} E_{x2} \\ E_{y2} \end{bmatrix} = \begin{bmatrix} \{E_{x1}\cos(\phi_2-\phi_1) - E_{y1}\sin(\phi_2-\phi_1)\}\exp(-\mathrm{i}\delta_2) \\ \{E_{x1}\sin(\phi_2-\phi_1) + E_{y1}\cos(\phi_2-\phi_1)\} \end{bmatrix}. \tag{3}$$

Finally, the sequential procedure defined in equations (2) and (3) continues to the last cubic cell in the column in order to obtain the tangential components of the electric field of the transmitted light through the NLC film, $E_{x\mathrm{n}}$ and $E_{y\mathrm{n}}$, respectively. The intensity of the exiting transmitted light I, taking into account the presence of the analyzer, is given by:

$$I = \left[E_{x\mathrm{n}}\sin(\phi_{\mathrm{n}}) - E_{y\mathrm{n}}\cos(\phi_{\mathrm{n}})\right] \times \left[E_{x\mathrm{n}}\sin(\phi_{\mathrm{n}}) - E_{y\mathrm{n}}\cos(\phi_{\mathrm{n}})\right]^{*}. \tag{4}$$

More specific details of the widely used aggregate method can be found in [15, 16, 25].

2.2. *The Berreman method*

Figure 2 summarizes the coordinate system and optical components used in Berreman's method. Two glass layers are placed between the crossed polarizers and the NLC film. The computational domain including the supporting glasses is divided into finite cubic lattices, as in the aggregate model.

The monochromatic incident light, which has the same complex time dependency $E=E_o\exp(i\omega t)$ as in the aggregate model, is introduced into the computational space at $z=0$. The direction of incident light is indicated by vertical arrows in figure 2. The entire medium can be approximated by a stack of homogeneous cubic lattices, since each lattice is assumed to be a homogenous medium.

The following set of linear differential equations for the tangential components of the electric and magnetic fields can be derived from Maxwell's equations:

$$\frac{d\Psi}{dz} = -i\frac{\omega}{c}\Delta(z)\Psi \quad \Psi = \left(E_x,\, H_y,\, E_y,\, -H_x\right)^T \quad (5)$$

where ω is the angular frequency, c is the velocity of light in vacuum, z is the propagation direction, $\mathbf{E}=(E_x,E_y)$ is the electric field, and $\mathbf{H}=(H_x,H_y)$ is the magnetic field vector. The matrix $\Delta(z)$ depends mainly on the dielectric constants, the birefringence, and the Euler angles of the local director **n**. The solution of the first order linear equation (5) can be expressed by:

$$\Psi_t(d) = F(\mathrm{i},\,\mathrm{n})\Psi_1(0) \quad (6)$$

$$\boldsymbol{F}(\mathrm{i},\,\mathrm{n}) = \boldsymbol{p}_{i+n}(h)\boldsymbol{p}_{i+n-1}(h)\ldots\ldots\boldsymbol{p}_{i+1}(h)\boldsymbol{p}_i(h). \quad (7)$$

The transmitted waves ψt are now obtained by use of the total transfer matrix $\boldsymbol{F}$. The polarization, the retardation, and the reflection of the incident light due to the variation of the optic axis and the existence of different media are computed in the total transfer matrix $\boldsymbol{F}$ within the computation domain in equation (7). The matrix $\boldsymbol{F}$ is obtained through multiplication of the local transfer matrix $\boldsymbol{p}_i$. The symbol $\boldsymbol{p}_i$ represents the local transfer matrix for the ith cubic lattice of thickness h. Within the thickness h, the medium is assumed to be homogeneous, so that the local transfer matrix $\boldsymbol{p}_i$ can be expressed by the following series:

$$\boldsymbol{p}_i(h) = \exp\left(i\frac{\omega}{c}\Delta h\right) = I + \frac{i\omega h}{c}\Delta + \frac{1}{2!}\left(\frac{i\omega h}{c}\right)^2\Delta^2 + \frac{1}{3!}\left(\frac{i\omega h}{c}\right)^3\Delta^3 + \ldots\ldots \quad (8)$$

Depending on the thickness h of the lattice, the higher order terms can be neglected in equation (8). The main challenge of the Berreman 4×4 method is to determine the transfer matrix $\boldsymbol{p}_i$ that relates the tangential components of the electrical and magnetic field from lattice i to lattice i+1. In our study, the local transfer matrix $\boldsymbol{p}_i$ (h) is obtained with the aid of the built-in function called 'expm' in Matlab 6.5 [29].

In the initial step of the computational light transmission, the vector $\psi_1(z=0)$ is divided into an incident wave and a reflected wave at the surface ($z=0$), given by:

$$\Psi_1 + \Psi_{in} + \Psi_r \quad (9)$$

where the subscripts in and r indicate the incident and reflected waves, respectively. The incident wave ψ_{in}, the reflected wave ψ_r, and the transmitted wave Ψ_t which describe the electric and magnetic tangential components, can be expressed in terms of electric field only, since the magnetic components are proportional to the corresponding orthogonal electric components, the proportionality constant being the refractive index of the medium which must be isotropic and of a non-magnetic ambient medium. The general expression of the three waves in the normal incident case is given by:

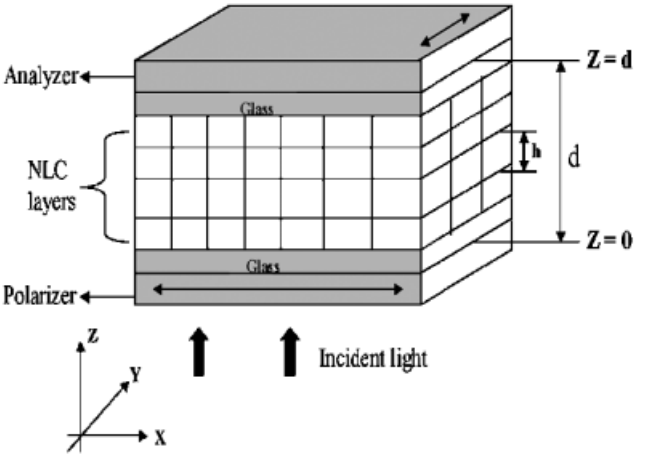

Figure 2. Schematic diagram of the computational domain between crossed polarizers for Berreman's method. The symbol h indicates the dimension of each cubic cell; d indicates the thickness of the computation domain in the light propagation (z) direction. Between the crossed polarizers and the LC layer, there are two thin glass substrates.

$$\Psi_t(d)=\begin{bmatrix} E_{xt} \\ n_t E_{xt} \\ E_{yt} \\ n_t E_{yt} \end{bmatrix} \quad \Psi_{in}(0)=\begin{bmatrix} E_{xin} \\ n_i E_{xin} \\ E_{yin} \\ n_i E_{yin} \end{bmatrix} \quad \Psi_r(0)=\begin{bmatrix} -E_{xr} \\ n_r E_{xr} \\ E_{yr} \\ -n_r E_{yr} \end{bmatrix} \tag{10}$$

where E_{xin} and E_{yin} are the known electric components of the incident wave, E_{xr}, E_{yr}, E_{xt} and E_{yt} are the electric tangential components of the reflected and the transmitted waves, respectively, and n indicates the refractive index. The incident waves E_{xin} and E_{yin} are linearly polarized by the ideal polarizer which is placed along the x direction. Based on the calculation shown in equation (6), the solution vectors given by the transmitted wave vectors E_{xn} and E_{yn} and the reflected wave vectors E_{xr} and E_{yr} can be obtained. The intensity of the transmitted wave is finally obtained after considering the presence of the ideal analyzer, which is placed along the y direction. Detailed mathematical descriptions of the Berreman 4×4 method can be found in [11, 26, 27].

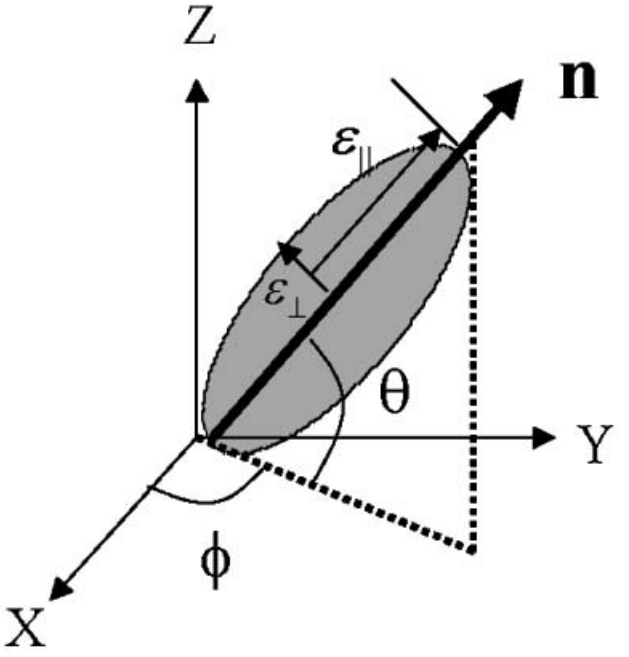

Figure 3. Euler angles (θ,ϕ) of optical dielectric tensor $\boldsymbol{\varepsilon}$ uniaxial ellipsoid with respect to the (x, y, z) coordinate system. The unit vector **n** is the local director. The parallel and transverse components of the dielectric tensor $\boldsymbol{\varepsilon}$ are also indicated.

2.3. *The FDTD method*

In this section we present the main features of the FDTD method, especially when applied to NLC media. Since the method has been widely described in the textbook literature [28], here we focus only on fundamental issues. Light propagation for non-magnetic materials is described by the solution to the following Maxwell curl equations together with the appropriate constitutive equations:

$$\frac{\partial \boldsymbol{D}}{\partial t}=\nabla\times\boldsymbol{H} \tag{11}$$

$$\frac{\partial \boldsymbol{B}}{\partial t}=-\nabla\times\boldsymbol{E} \tag{12}$$

$$\boldsymbol{D}=\varepsilon\boldsymbol{E} \tag{13}$$

$$\boldsymbol{B}=\mu_o\boldsymbol{H}. \tag{14}$$

The dielectric tensor $\boldsymbol{\varepsilon}(x, y, z)$ can be written in terms of the Euler angles: the tilt angle $\theta(x, y, z)$ and the azimuthal angle $\phi(x, y, z)$ [6]. Figure 3 shows the optic axis (**n**), the Euler angles (θ,ϕ), the ordinary dielectric constant $\varepsilon_\perp$, and extraordinary dielectric constant $\varepsilon_\parallel$, the latter being the components of the dielectric tensor $\boldsymbol{\varepsilon}$.

After proper transformation, the optical dielectric tensor $\boldsymbol{\varepsilon}$ for a uniaxial medium is expressed by:

$$\boldsymbol{\varepsilon}=\begin{pmatrix} \varepsilon_\perp+\Delta\varepsilon\cos^2\theta\cos2\phi & \Delta\varepsilon\cos^2\theta\sin\phi\cos\phi & \Delta\varepsilon\sin\theta\cos\theta\cos\phi \\ \Delta\varepsilon\cos^2\theta\sin\phi\cos\phi & \varepsilon_\perp+\Delta\varepsilon\cos^2\theta\sin2\phi & \Delta\varepsilon\sin\theta\cos\theta\sin\phi \\ \Delta\varepsilon\sin\theta\cos\theta\cos\phi & \Delta\varepsilon\sin\theta\cos\theta\sin\phi & \varepsilon_\perp+\Delta\varepsilon\sin^2\theta \end{pmatrix} \tag{15}$$

where $\Delta\varepsilon=\varepsilon_\perp-\varepsilon_\parallel$. Scaling the Maxwell's curl equations (11–14) using $\widetilde{D}=1/(\varepsilon_o\mu_o\boldsymbol{D})^{\frac{1}{2}}$ and $\widetilde{E}=\left(\frac{\varepsilon_o}{\mu_o}\right)^{\frac{1}{2}}$ gives [30]:

$$\frac{\partial\widetilde{\boldsymbol{D}}}{\partial t}=\frac{1}{(\varepsilon_o\mu_o)^{\frac{1}{2}}}\nabla\times\boldsymbol{H} \tag{16}$$

$$\widetilde{\boldsymbol{D}}=\varepsilon^*\widetilde{\boldsymbol{E}} \tag{17}$$

$$\frac{\partial \boldsymbol{H}}{\partial t} = -\frac{1}{(\varepsilon_o \mu_o)^{\frac{1}{2}}} \nabla \times \tilde{\boldsymbol{E}} \tag{18}$$

where **D** is the electric flux, μ_o is the free space magnetic permeability, and ε^* is the relative dielectric term which can include dispersive or nonlinear material properties [31]. In our study, NLCs are assumed to be non-magnetic. The purpose of the normalization of the Maxwell curl equations and of using the electric flux **D** instead of the electric **E** field, as expressed in equations (16–18), is to implement an unsplit perfectly matched layer (PML) for an anisotropic medium in a simple way, and also to implement the PML regardless of level of complexity in the optical properties of the medium; the PML concept is explained below. From now on, it will be assumed that we are referring to normalized values.

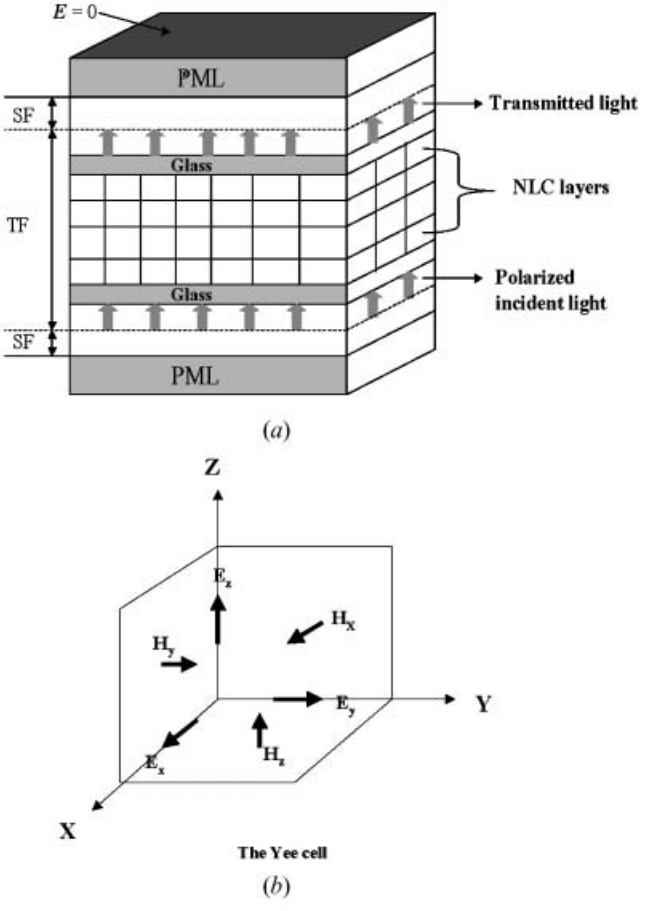

Figure 4. Definition of the computational domain and the Yee cell used in the FDTD method. (*a*) TF and ST are the total field and the scattered field respectively. Periodic boundary conditions are used in x and y directions. The E_x and E_y components are zero in the last layer of the PML. (*b*) E_x, E_y, E_z, H_x, H_y, and H_z are the electric and magnetic components in the rectangular (x, y, z) coordinate system.

The general computational domain for the FDTD method is shown in figure 4 (*a*). The Yee cell [17] as shown in figure 4 (*b*), which consists of the electric and magnetic components in a cubic lattice, is used to fill the three-dimensional computation domain. In the Yee algorithm, every **E** and **H** component is surrounded by the four circulating **H** and **E** components, respectively [28]. Since both electric and magnetic fields in time and space are solved using the coupled Maxwell's equations rather than the electric field alone, the Yee algorithm consisting of the **E** and **H** components in a staggered grid provides a more robust solution for a wave propagation [28].

Second order central finite differences are used to discretize the Maxwell's equations (16–18) in both space and time. 3D spatial discretization follows the Yee cell. For temporal discretization, a fully explicit leapfrog scheme is used to update the **E** and **H** field in half time increments, respectively [18, 30]. For example, the x component of the dielectric displacement D_x and the magnetic field H_x are updated by the expression:

$$D_x|_{i,j,k}^{n+1} = D_x|_{i,j,k}^{n-1} + \frac{\Delta t}{(\varepsilon_o \mu_o)^{\frac{1}{2}}} \left(\frac{H_z|_{i,j+1,k+1/2}^{n+1/2} - H_z|_{i,j+1,k-1/2}^{n+1/2}}{\Delta y} - \frac{H_y|_{i,j+1,k+1}^{n+1/2} - H_z|_{i,j+1/2,k+1}^{n+1/2}}{\Delta z} \right) \tag{19}$$

$$E_x\Big|_{i,j,k}^{n+1} = \varepsilon^*(i,j,k)^{-1} D_x\Big|_{i,j,k}^{n+1} \tag{20}$$

$$H_x|_{i-1/2,j+1,k+1}^{n+1/2} = H_x|_{i-1/2,j+1,k+1}^{n-1/2} + \frac{\Delta t}{(\varepsilon_o \mu_o)} \left(\frac{E_y|_{i-1/2,j+1,k+3/2}^{n} - E_y|_{i-1/2,j+1,k+1/2}^{n}}{\Delta z} - \frac{E_z|_{i-1/2,j+3/2,k+1}^{n} - E_z|_{i-1/2,j+1/2,k+1}^{n}}{\Delta y} \right) \tag{21}$$

where i, j, k indicate the x, y and z components in the rectangular coordinate system and Δt, Δy and Δz are the time and space increments, respectively. The dielectric displacement components are updated using the values of the magnetic components which have advanced with the $\Delta t/2$ increment. The electric components, which are assumed to be located at the same grid points as the dielectric displacement components, are obtained through the expression of equation (20). In this step, the anisotropic properties of the system are imposed.

Now, the obtained electric components are used in order to update the magnetic components advancing in the $\Delta t/2$ increment [14, 18]. The electric and magnetic components are advanced in time until a desirable steady-state is reached. Full details of the algorithm can be found in [28].

In the FDTD method, a total field and scattered field (TF/SF) formulation is employed in order to generate a monochromatic plane wave into the computational domain. In this formulation, the computational domain is separated into two regions as shown in figure 4. A linearly polarized incident plane wave after implementing the ideal polarizer, parallel to the x direction, is introduced on the lower interface between the TF and SF region in the xy plane. The linearly polarized light propagates through the glass layer and the NLC medium based on the FDTD computational scheme. Due to the existence of the different media and the variation of the NLC orientation, the linearly polarized incident wave undergoes scattering, reflections, and retardations. In the TF region, the incident wave and the scattered wave are calculated according to equation (22), and in the SF region only the scattered wave is calculated according to equation (23) [28, 30]:

$$\begin{aligned} E_{\text{total}} &= E_{\text{inc}} + E_{\text{scat}} \\ H_{\text{total}} &= H_{\text{inc}} + H_{\text{scat}} \end{aligned} \tag{22}$$

$$\begin{aligned} E_{\text{scat}} &= E_{\text{total}} - E_{\text{inc}} \\ H_{\text{scat}} &= H_{\text{total}} - H_{\text{inc}} \end{aligned} \tag{23}$$

where $\mathbf{E}_{\text{total}}$ and $\mathbf{H}_{\text{total}}$ are the electric and magnetic components in the total region, $\mathbf{E}_{\text{inc}}$ and $\mathbf{H}_{\text{inc}}$ are the electric and magnetic components of the incident wave, and $\mathbf{E}_{\text{scat}}$ and $\mathbf{H}_{\text{scat}}$ are the electric and magnetic components of the scattered wave due to the presence of different media and the variation of the NLC orientation. The TF/SF formulation based on the linearity of Maxwell's equations overcomes the difficulties and limitations of conventional formulations such as a hard source which causes a spurious and non-physical retro-reflection back toward the material of interest [28]. The TF/SF formulation approach can easily generate an arbitrary propagation direction, polarization, time waveform, and duration; for more details see [28].

One important aspect for the implementation of the FDTD is to apply efficient and effective boundary conditions to truncate the computational domain without reflecting outgoing waves back into the domain. The perfectly matched boundary layers (PMLs) have shown the best performance over conventional absorbing boundary conditions (ABC), such as the Mur ABC, for both isotropic and anisotropic media [14, 19, 28]. In the PML, boundary layers, which have fictitious exponential conductivities varying along the normal to the tangential electric components, surround the computational domain of interest. Any arbitrary waves from the domain enter the PML layers through the interface between the PML layer and the domain of interest with no reflection, regardless of angle of incidence and medium types. The entering waves are attenuated exponentially due to the exponential conductivities normal to the interface [14, 19, 28]. In other words, the PML is an artificial medium which absorbs all waves leaving the computational space of interest without reflecting the waves back into that space. Therefore, the PML provides no numerical artificial reflections that result from truncating the computational domain. In order to implement the PML for an anisotropic medium such as NLCs, the magnetic field **H** and the electrical displacement **D** are used instead of the electric field **E** in order to avoid the difficulties arising from employing the reflectionless interface for the anisotropic medium. The formulation for the PML has been successfully utilized for LC applications [13, 14, 23]. In spite of accuracy and robustness of the PML in FDTD, one difficulty arises from splitting the components of the **D** and **H** fields. In the three-dimensional case, the six components of the **D** and **H** fields yield 12 subcomponents denoted as D_{xy}, D_{xz}, D_{yz}, D_{yx}, D_{zx}, D_{zy}, H_{xy}, H_{xz}, H_{yz}, H_{yz}, H_{zx}, H_{zy} [32]. For example, the D_z term and H_z are split follows:

$$\frac{\partial D_{zx}}{\partial t} = \sigma_x D_{zx} = \frac{\partial \left(H_{yz} + H_{yz}\right)}{\partial x} \tag{24}$$

$$\frac{\partial D_{zy}}{\partial t} = \sigma_y D_{zy} = -\frac{\partial \left(H_{xy} + H_{xz}\right)}{\partial y} \tag{25}$$

$$\frac{\partial H_{zx}}{\partial t} = \sigma_x^* H_{zx} = -\frac{\partial \left(D_{yz} + D_{yx}\right)}{\partial x} \tag{26}$$

$$\frac{\partial H_{zy}}{\partial t} = \sigma_y^* H_{zy} = \frac{\partial \left(D_{xy} + D_{xz}\right)}{\partial y} \tag{27}$$

where the parameters σ_x, σ_y, σ_x^*, and σ_y^* are the PML conductivities for the dielectric displacement and the magnetic field, respectively. These equations reduce to the initial Maxwell's equations where the PML conductivities are equal to zero. Consequently, additional computational resources are required for the PML implementation. A simplified PML formulation without splitting the involved **D** and **H** components is called the unsplit PML method and has been proposed and successfully implemented in 2D and 3D problems, for isotropic and anisotropic media [30, 33]. In our study,

the unsplit PML method is used to truncate the computational domain. For example, the expression of the unsplit PML in the x direction after meeting two requirement conditions is given by [33]:

$$j\omega\left(1+\frac{\sigma(x)}{i\omega\varepsilon_o}\right)^{-1} D_x = c_o\left(\frac{\partial H_z}{\partial y}-\frac{\partial H_y}{\partial z}\right) \quad (28)$$

$$j\omega\left(1+\frac{\sigma(x)}{i\omega\varepsilon_o}\right) D_y = c_o\left(\frac{\partial H_x}{\partial z}-\frac{\partial H_z}{\partial x}\right) \quad (29)$$

$$j\omega\left(1+\frac{\sigma(x)}{i\omega\varepsilon_o}\right) D_z = c_o\left(\frac{\partial H_y}{\partial x}-\frac{\partial H_x}{\partial y}\right) \quad (30)$$

where $\sigma(x)$ is the PML conductivity with respect to the x direction. In addition, the tangential components of the electric field are zero in the last layer of the PML, as required by the perfect conductor boundary condition. The performance and stability of the unsplit PML are well described in [30].

When the computational domain is completely surrounded by the supporting glasses and the PML layers, this leads to generation of undesirable artificial ringing at the corners of the structure due to artificial diffractions of the incident wave at these corners, as pointed out in [13, 22]. An alternative form for the boundary conditions is to use periodic boundary conditions (PBC) in the transverse, x and y directions instead of the PML [13, 14, 23]. The PML are implemented in the light propagation z direction, parallel to the supporting glasses and the PBC are implemented in transverse, x and y directions.

The magnitude and phase of the electric and magnitude field are obtained after a sufficient time delay until the steady state optical response is reached.

3. Computational modelling results

Numerical applications of the FDTD method will be carried out for two general cases: (i) singular line defects, known as thins [34], and (ii) a non-singular line defect, known as thicks [34]. In our study, the optical simulations will be focused on the vicinity of the defect cores in which a high rate of spatial variations of the anisotropic dielectric tensor is observed in the lateral directions. The same singular and non-singular director fields used for the optical simulations using the aggregate model [15], will be considered in our study in order to compare it with the FDTD and Berreman methods. The singular and non-singular director fields used in the optical computations are solutions to the classical equations of nematostatics using the one-constant approximation and are discussed by de Gennes and Prost [34].

3.1. *Singular line defects*

Using a rectangular (x, y, z) coordinate system, a wedge disclination line along the z direction is described by a planar director field of the form [15, 34].

$$n(x, y) = (n_x, n_y, 0) = (\cos\phi(x, y), \sin\phi(x, y), 0),$$
$$\phi = s\tan^{-1}\left(\frac{y}{x}\right) + c \quad (31)$$

where ϕ is the angle between the local director and the x axis, c is a constant and s represents the strength of the disclination. The sign of s denotes the sense of director rotation when encircling the defect, and the magnitude of s describes the amount of rotation. The values of s are quantized: $s=\pm 1/2,\ \pm 1,\ \pm 3/2,\ \ldots$, and since the elastic energy of the defect scales with s^2, lower index defects are observed [34]. For optical calculations the important features of the singular lines are: (i) the length scale associated with the defect core is a grid point—in reality the defect core radius r_c has dimensions in the nano-scale and much smaller than the wavelength of light used in polarizing optical

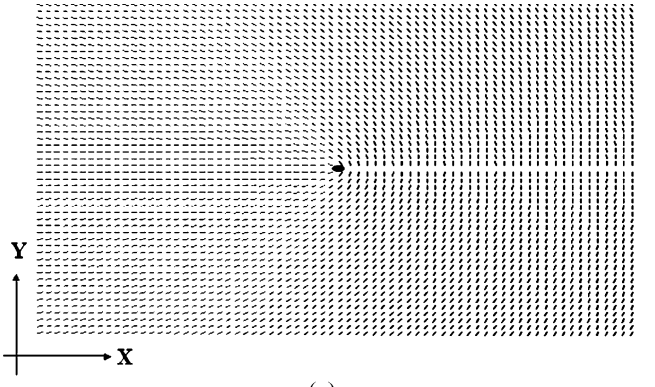

(*a*)

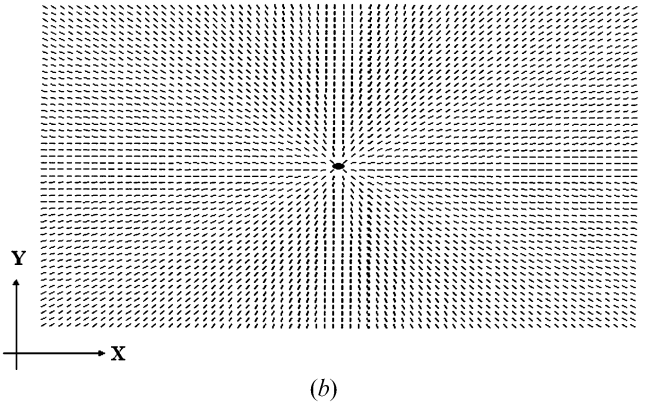

(*b*)

Figure 5. Director profiles in the xy plane for singular disclination lines, of strength (*a*) $s=+1/2$ and (*b*) $s=+1$. The director field is planar: $n_z=0$.

microscopy; (ii) the director gradients that affect the optical output $\mathbf{n}/x$ and $\mathbf{n}/y$ increase towards the core of he defect; (iii) the director field is 2D planar ($n_z=0$) and always normal to the propagation direction, (iv) besides the nanoscopic core, there is no characteristic length scale in the director field.

Figure 5 shows visualizations of the singular director field for: (*a*) $s=+1/2, c=0$, and (*b*) $s=+1, c=0$, computed using equation (31). Optical simulations for these two NLC structures are computed using the FDTD, the aggregate, and the Berreman methods, with a computational grid consisting of $70\times50\times20$ rectangular Yee cells. For the FDTD method, extra Yee cells are added along the x and y directions in order to compensate for the imposed PBCs, and along the z direction to accommodate for the supporting glasses and the unsplit PML formulation. An incident monochromatic plane wave with free wavelength $\lambda=633$ nm is generated on the lower interface in the xy plane between the TF and SF region in the normal incident case. The spatial discretization is characterized by a grid size equal to $\lambda/20$, which is equivalent to $\Delta x=\Delta y=\Delta z=31.65$ nm, and a dimensionless time step of $\Delta t=5.2787\times10^{-17}$ s is considered. The uniaxial NLCs with ordinary refractive index, $n_0=1.5$ and extraordinary refractive index, $n_e=1.7$ are considered; these are typical NLC values [16]. The ordinary refractive index of the supporting glasses is assumed to be equal to the ordinary refractive index of the NLC. In addition, the NLC and the supporting glasses are assumed to be lossless and non-magnetic.

Figures 6 and 7 show 2D (xy) grey scale computed normalized optical images from the $s=+1/2$ and $s=+1$ singular defects [shown in figures (5*a*,*b*)], respectively, according to (*a*) the aggregate model, (*b*) Bereman's method, and (*c*) FDTD. The direction of the polarizer is along the x axis and the direction of the analyzer is along the y axis. The vertical scales indicate the magnitudes of the normalized optical signal. The two crossed polarizers are considered to be ideal. The implementation of the ideal polarizers is employed according to [14]. The analyzer is implemented after the steady-state response of the electric and magnetic field is obtained.

Figures 6 and 7 show that the three optical methods capture the typical brush features observed in NLC under crossed polarizers, where the number of dark brushes is equal to four times the absolute value of the defect strength $|s|$ [34]; in figure 6 there are two brushes because $s=1/2$, while in figure 7 there are four brushes because $s=1$. The optical images of the two singular defects obtained using the aggregate model are in good agreement with the results of Nicholson [15]. The Berreman method generates the same optical images as the aggregate model due to the similar assumptions of the two matrix–type methods in the normal incidence case. Unlike the matrix-type methods, the FDTD method generates the cross–dark band through the defect core, as shown in figures 6(*c*) and 7(*c*), which is not observed in the matrix-type methods. This cross–dark band optical image is in agreement with the experimental optical images shown in figure 12.6 of ref. [4] for $s=1$ and $s=1/2$ disclination lines.

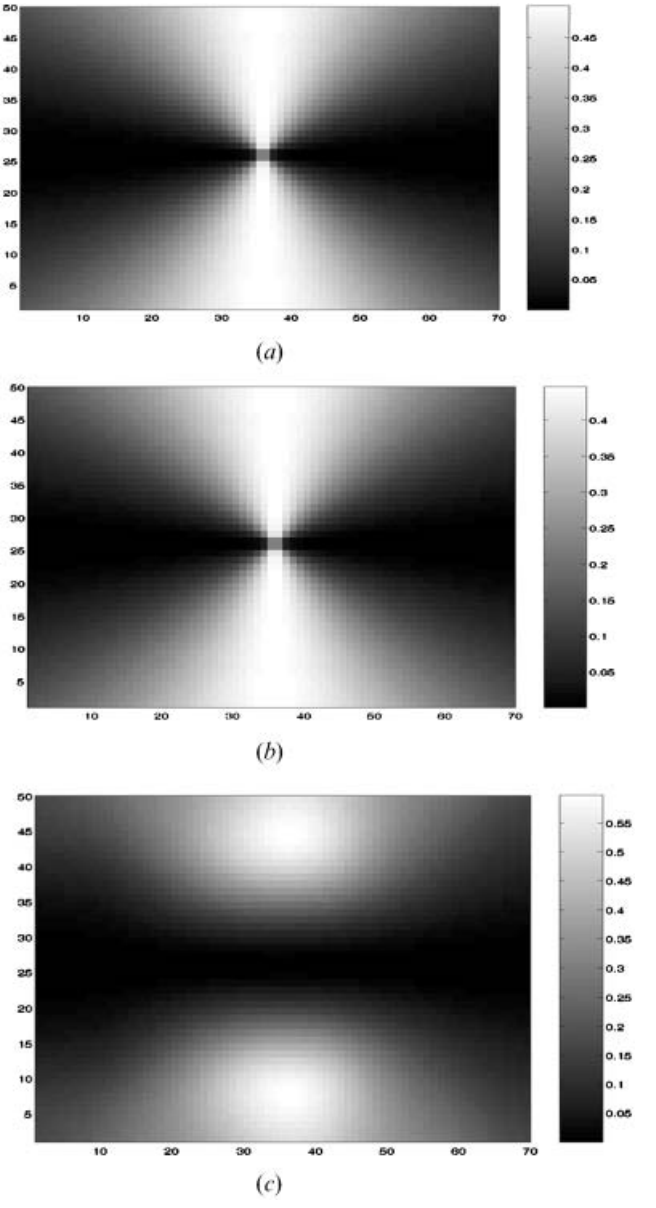

Figure 6. Optical images of the normalized intensity of the transmitted light in the normal incidence case for $s=+1/2$: (*a*) the aggregate model, (*b*) Berreman's method, and (*c*) FDTD method.

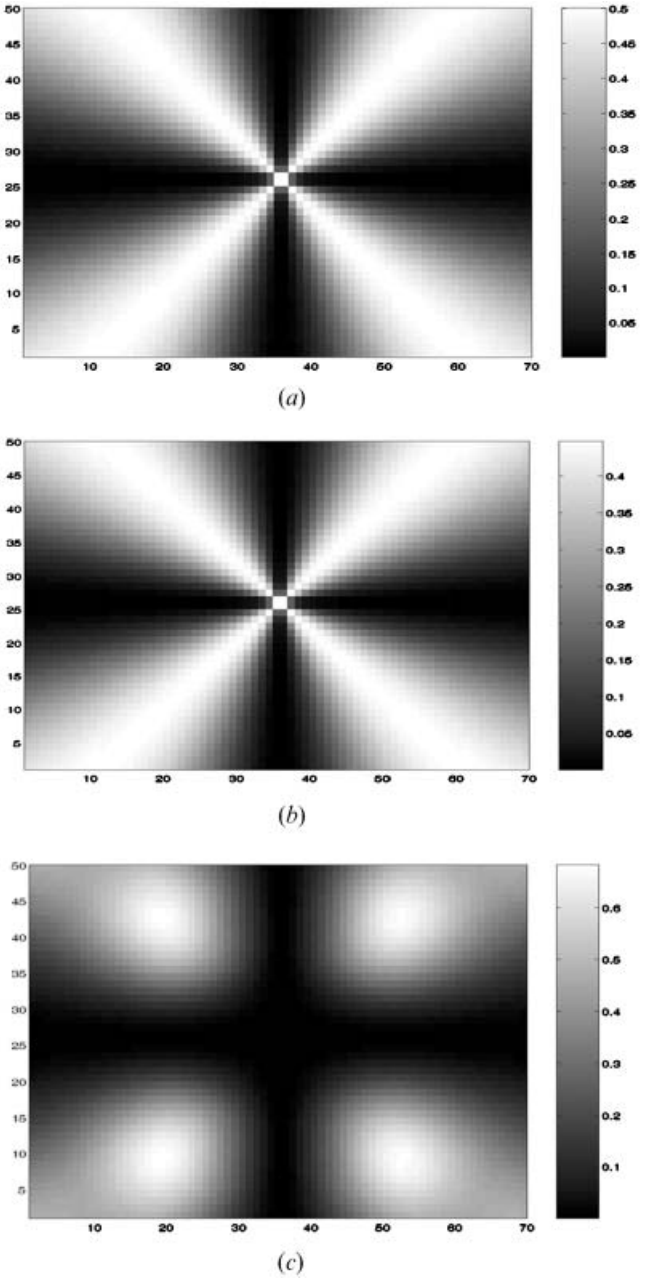

Figure 7. Optical images of the normalized intensity of the transmitted light in the normal incidence case for $s=+1$: (*a*) the aggregate model, (*b*) Berreman's method, and (*c*) FDTD method.

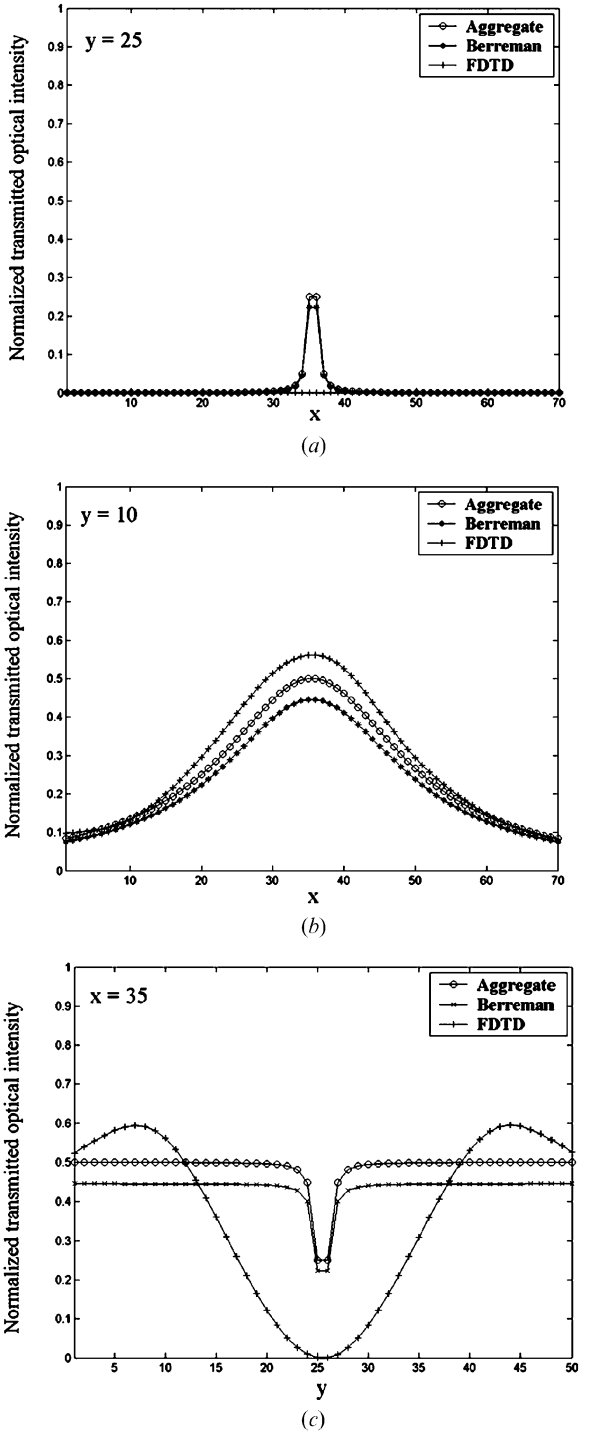

Figure 8. Normalized transmitted optical intensity NOI profiles from the three optical methods for the $s=+1/2$ singular defect: for (*a*) NOI as a function of x, $y=25$; (*b*) NOI as a function of x, $y=10$; and (*c*) NOI as a function of y, $x=35$. The specific values of x and y indicate the node number of the grid for the LC films. The defect line is located at $(x, y)=(36,26)$.

To quantify the differences between the three methods the normalized optical intensity (NOI) was computed and further analyzed. For brevity we use the following nomenclature to identify the NOIs: NOI_{ag} refers to the aggregate model, NOI_B to Berreman's, and NOI_F to the FDTD method. Figures 8 and 9 show the following set of NOI_{ag}, NOI_B and NOI_F profiles: (*a*)

NOI as a function of distance along the x direction for $y=25$, (b) NOI as a function of distance along the x direction for $y=10$, and (c) NOI as a function of distance along the y direction for $x=35$, corresponding to Figures 6 and 7. The specific x and y values correspond to the node number in the computational domain. The defects are located at: $(x, y)=(36,26)$.

The figures indicate that the two matrix-type methods show slightly different results in the transmitted optical intensity, because the aggregate model introduced by Nicholson [15] cannot capture multiple reflections between the different media, for instance, air to glass and glass to LCs. The figures show that the optical images of the transmitted light obtained between the two matrix-type methods and FDTD do not match, as already shown in figures 6 and 7, especially in the central defect region. Figure 8 (c) shows that the matrix methods display a narrow pulse signal, while the FDTD displays a diffuse wave, which explains the presence of the tick brush at the defect. Likewise figure 9 (c) shows that the matrix methods predict a pulse which is absent in the FDTD signal. The strong disagreement between the Berreman and FDTD methods in the central defect region is due to lateral $\mathbf{n}/x$ and $\mathbf{n}/y$ gradients of the director field. These computations show that the FDTD method captures additional information on the lateral scattering effects in the LC structures that is not captured by the matrix methods. A similar trend in the 2D case is reported between the Berreman and FDTD methods in [13, 23] due to the presence of significant lateral director gradients. As expected and confirmed by the present computations, the matrix-type and FDTD methods predict similar results in the boundary regions where lateral gradients in the director field are weak. Figures 6 (c) and 8 (c) show that the optical images of the FDTD method have a characteristic length scale associated with the wavelength λ of the incident light (one grid size is $\lambda/20$). In figure 6 (c) the characteristic feature is the horizontal central band of thickness l, and in figure 8 (c) it is the central dark circle of radius λ. Figures 8 and 9 show that the maximum difference between NOI_{ag}, NOI_B, and NOI_F is at the defect core $(x, y)=(36,26)$, where lateral director gradients are largest.

One of the properties of the FDTD method is that derivatives of the polar and azimuthal angles with respect to the transverse directions are taken into account. A non-symmetrical FDTD curve is therefore observed in contrast to the matrix-type methods [23, 33]. However, the non-symmetrical FDTD curve reported in [23, 33] is not observed in our study because there is no change in the sign of derivatives ϕ/x and ϕ/y in the transverse directions.

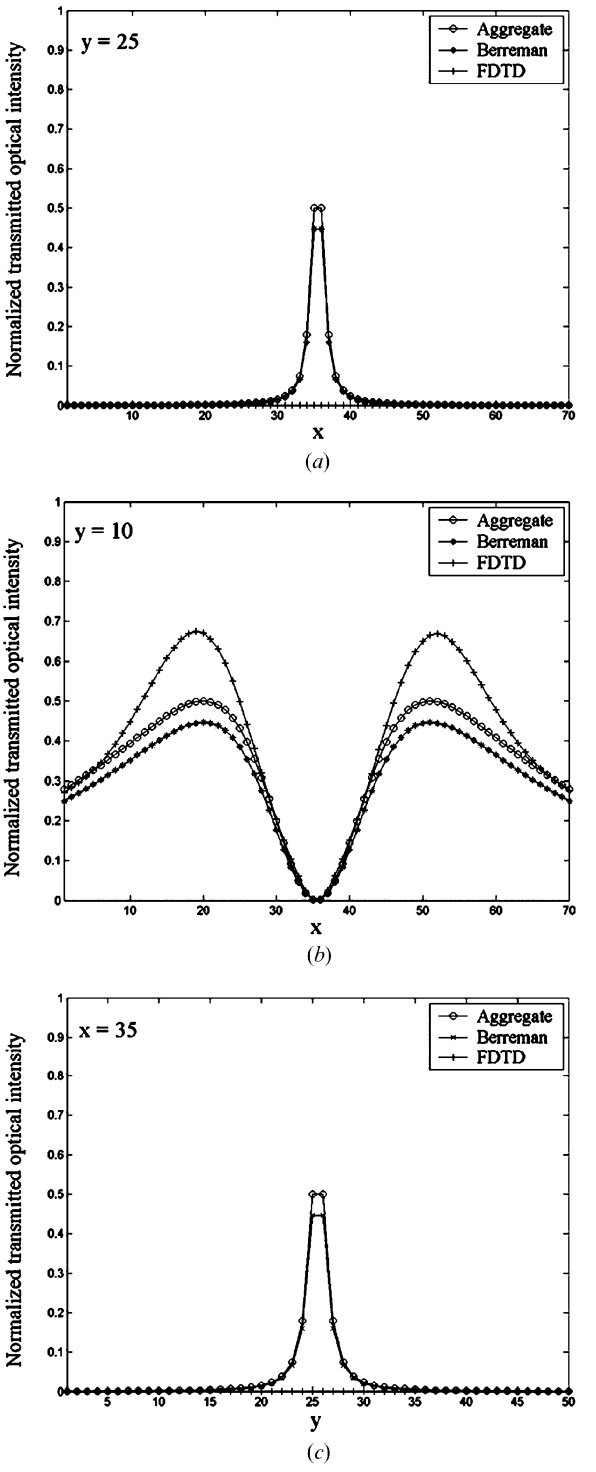

Figure 9. Normalized transmitted optical intensity NOI profiles predicted by the three optical methods for the $s=+1$ singular defect: for (a) NOI as a function of x, $y=25$; (b) NOI as a function of x, $y=10$; and (c) NOI as a function of y, $x=35$. The specific values of x and y indicate the node number of the grid for the LC films. The defect line is located at $(x, y)=(36,26)$.

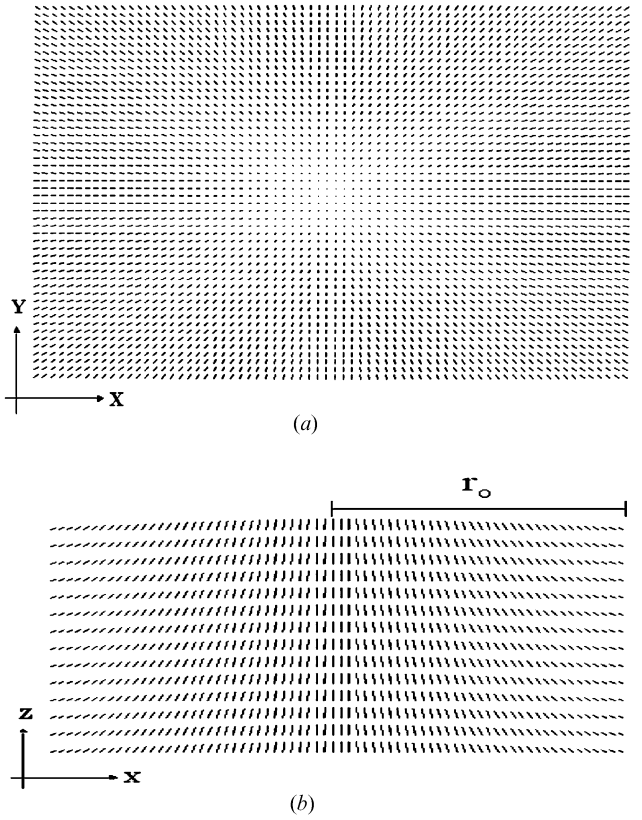

Figure 10. Director profiles in the xy plane for non-singular disclination lines: (*a*) $s=+1$; (*b*) the director field is non-planar, and the director escapes into the third (z) dimension.

3.2. *Non-singular line defects*

A non-singular defect of strength $s=+1$, shown in figures 10 (*a*,*b*), emerges when the director escapes into the third dimension in order to lower the total elastic energy [34], giving rise to experimentally observed so-called thick lines. Figure 10 (*a*) shows a transverse cut with respect to the non-singular core of strength $s=+1$ which aligned along the z direction. The projection of the director field on the xy plane is radial and axisymmetric. Figure 10 (*b*) shows a side view, showing how the director tilts away from the z direction as the radial distance from the non-singular core increases. The axisymmetric NLC structure of the non-singular defect can be expressed in a rectangular (x, y, z) coordinate system by [26]:

$$\begin{aligned} n(x,y) &= \big(n_x(x,y), n_y(x,y), n_z(x,y)\big) = \\ &\quad (\cos\phi\cos\theta, \sin\phi\cos\theta, \sin\theta)\phi = \\ s\tan^{-1}\left(\frac{y}{x}\right),\ \theta &= 2\tan^{-1}\left(\frac{r_o}{r}\right) - \frac{\pi}{2}, \quad r^2 = x^2 + y^2 \end{aligned} \tag{32}$$

where θ is the director tilt angle measured from the z axis, ϕ is the director twist angle measured from the x axis, r is the distance from the core, and r_o is the radial distance form the defect axis. The tilting of the director away from the xy plane is characterized by two values:

$$\text{for } r=0,\ \theta=\pi/2;\ \text{for } r=r_o,\ \theta=0. \tag{33}$$

For optical calculation the important features of the non-singular lines are: (i) the length scale associate with the defect r_0—in reality r_0 has dimensions in the micron-scale and is of the order of magnitude of the wavelength of light used in polarizing optical microscopy; (ii) the director gradients that affect the optical output are $\mathbf{n}/x$ and $\mathbf{n}/y$; (iii) the director field is 3D ($n_z \neq 0$). The main difference in the director field between the singular and non-singular $s=+1$ lines is the director tilting effect and the length scale of the defect core.

The optical simulation of the non-singular defect mentioned were carried out by the FDTD, the aggregate and Berreman's methods. All optical simulations for the non-singular line defects were carried out using the same procedure and the same parameters used for the optical simulations of singular line defects in the previous section.

Figure 11 shows the optical images for an $s=+1$ non-singular defect according to (*a*) aggregate model, (*b*) Berreman's method, and (*c*) the FDTD method. The images correspond to the typical Maletese cross. The optical image of the non-singular case obtained using the aggregate model is in good agreement with the results by Nicholson [15]. Figure 11 shows that in contrast to the singular $s=+1$ defect, the FDTD method generates optical images geometrically similar to the two matrix-type methods, due to the homeotropic orientational structure in the central region around the core, where the transmitted light is therefore extinguished by the analyzer and where the stratified assumption can be justified. The main difference between the FDTD image and the matrix method images is that the Maletese cross in the latter has expanded.

It is expected that the two matrix-type methods, aggregate and Berreman, generate similar optical images and there is little magnitude difference in the normalized transmitted optical intensity, because the multiple reflections between the different media are not taken into account in the aggregate model, as explained in the previous section and shown in figure 12. In contrast to the previous results, the FDTD method generates similar optical images to the two matrix-type methods, as shown in figure 11, due to the director tilting in the central region around the core, where the transmitted light is therefore extinguished by the analyzer and the stratified assumption can be justified.

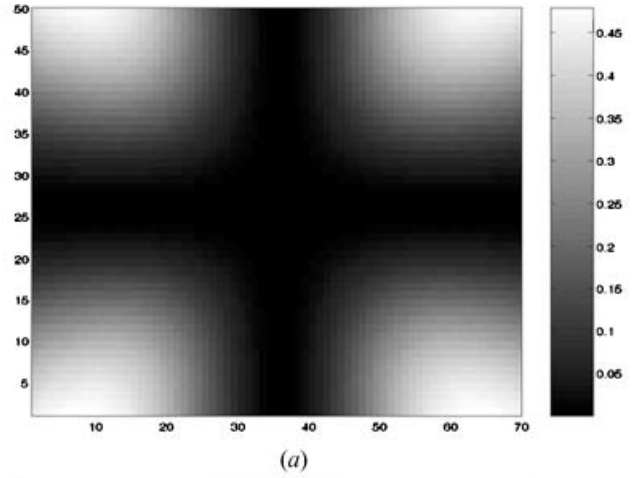

(*a*)

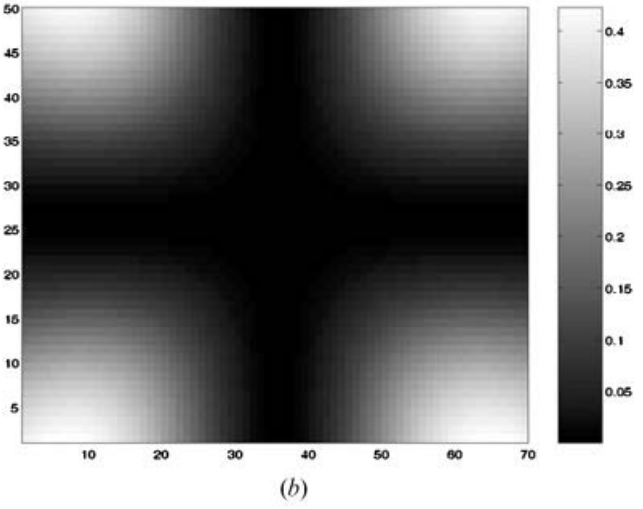

(*b*)

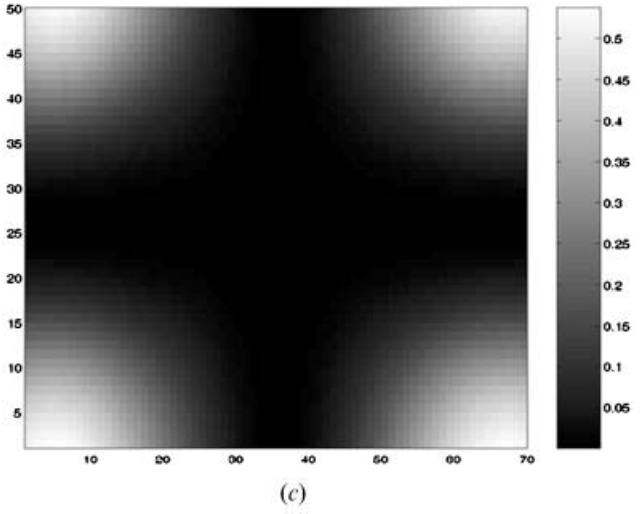

(*c*)

Figure 11. Optical images of the normalized intensity of the transmitted light in the normal incidence case for the $s=+1$ non-singular defect: (*a*) the aggregate model, (*b*) Berreman's method, and (*c*) the FDTD method.

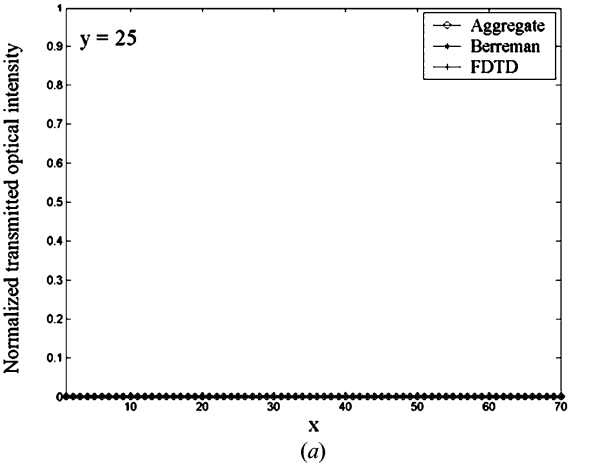

(*a*)

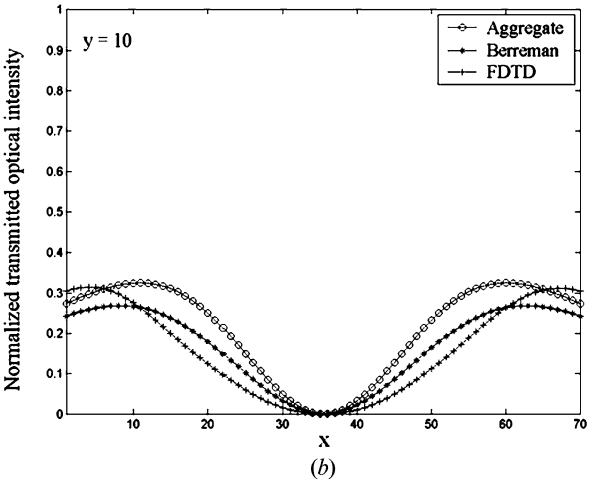

(*b*)

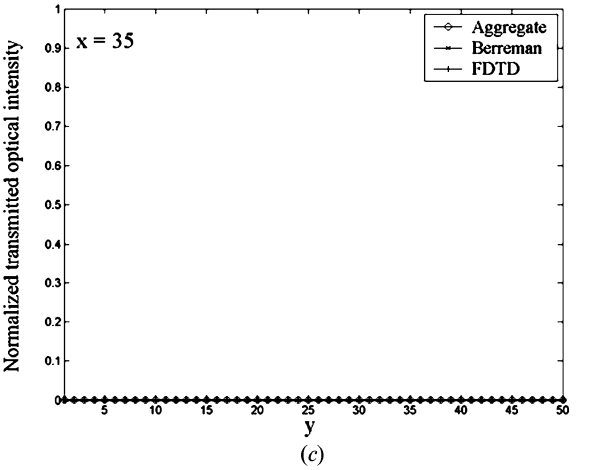

(*c*)

Figure 12. NOI profiles predicted by the three optical methods for the $s=+1$ non-singular defect: for (*a*) NOI as a function of x, $y=2$; (*b*) NOI as a function of x, $y=13$; and (*c*) NOI as a function of y, $x=66$. The specific values of x and y indicate the node number of the grid for the LC films. The defect line is located at $(x, y)=(36,26)$.

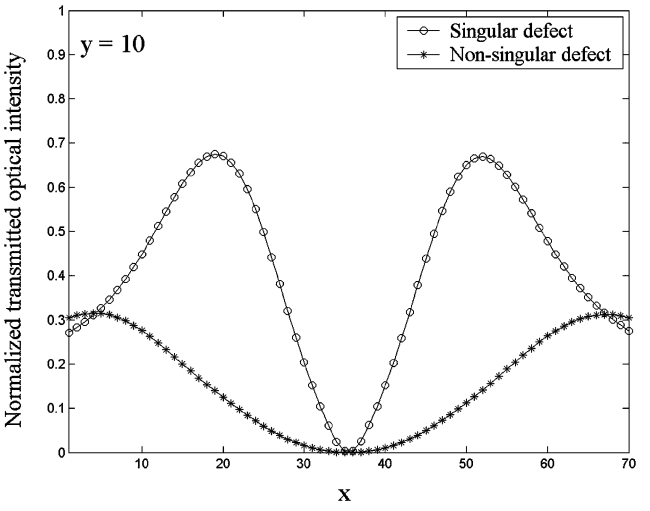

Figure 13. NOI as a function of x, $y=10$ predicted by the FDTD method for the $s=+1$ singular and non-singular defects. Deviations between the two signals increase away from the defect core. The director field of the singular defect has no characteristic length, but the optical signal has a characteristic scale equal to the wavelength of the incident light. The director field of the non-singular defect has a characteristic length greater than the wavelength of the incident light, and the optical signal has a characteristic scale equal to the director field length scale.

Disagreement between the matrix-type and the FDTD methods appears toward the boundary region where the director tilting disappears. In other words the director tilting weakens the lateral gradient effect. This weaking effect is at a minimum far from the defect and maximum at the defect core. In figure 12 we see that the three signals overlap at the defect core, and that the deviations grow with distance from the core.

Lastly, we compare the optical output from singular and non-singular $s=+1$ defect lines, briefly discussed in connection with figures 6 (c) and 7 (c). Figure 13 shows the NOI as a function of x, at $y=10$, computed using the FDTD method. The signal from the singular defect shows a large amplitude double pulse, while the non-singular defect produces a diffuse small amplitude single pulse. The characteristic length scale in the signal of the non-singular defect is the width of the computational domain, and corresponds to the length scale associated with the defect core region, r_o. On the other hand the characteristic length scale of the signal from the singular defect is approximately 20 length units, which corresponds to the wavelength of the incoming light source. The FDTD method is an efficient computational scheme to detect defect types and of high sensitivity to complex non-planar director fields.

4. Conclusions

Three-dimensional optical simulations for singular and non-singular line defects have been performed using the aggregate model, the Berreman's method, and the FDTD method; the former are algebraic matrix methods while the latter is based on numerical solutions to the Maxwell partial differential equations. The implementation complexity of the FDTD method is more than compensated by the sensitivity of the computed optical intensity to lateral director gradients in the plane normal to the direction of incident light. While the matrix methods are insensitive to lateral director gradients, and over predict light transmission in the immediate vicinity of singular defects, the FDTD method predicts no transmission, in agreement with experiments. In addition, when comparing singular and non-singular line defects, the FDTD method is highly sensitive to the director escape into the third dimension, thus being capable of differentiating planar from non-planar director fields. These features of the FDTD method are highly relevant to the further development of LC biosensors and to the use of rheo-optics to characterize liquid crystalline polymers.

Acknowledgements

This work is supported by a grant from the Donors of The Petroleum Research Fund (PRF) administered by the American Chemical Society. DkH acknowledges support from the Natural Science and Engineering Research Council of Canada.

References

[1] E. Lueder. *Liquid Crystal Displays: Addressing Schemes and Electro-optical Effects*. John Wiley, Chichester (2001).
[2] J.J. Skaife, N.L. Abbott. *Langmuir*, **17**, 5595 (2001).
[3] J.J. Skaife, N.L. Abbott. *Langmuir*, **16**, 3529 (2000).
[4] M. Kleman, O.D. Lavrentovich. *Soft Matter Physics: An Introduction*. Springer Verlag, London (2002).
[5] R.C. Jones. *J. opt. Soc. Am.*, **31**, 488 (1941).
[6] D.W. Berreman. *J. opt. Soc. Am.*, **62**, 502 (1972).
[7] P. Yeh. *J. opt. Soc. Am.*, **72**, 507 (1982).
[8] D.K. Yang, X.D. Mi. *J. Phys. D: appl. Phys.*, **33**, 672 (2000).
[9] E.E. Kriezis, S. Elston. *Mol. Cryst. liq. Cryst.*, **359**, 289 (2001).
[10] C. Gu, P. Yeh. *Displays*, **20**, 237 (1999).
[11] K.H. Yang. *J. appl. Phys.*, **68**, 1550 (1990).
[12] J.P. Park, G. Ryu, J. Byun, H. Hwang, S.T. Kim, I. Kim. *Opt. Rev.*, **9**, 207 (2002).
[13] E.E. Kriezis, S.J. Elston. *Opt. Commun.*, **177**, 69 (2000).
[14] E.E. Kriezis, S.K. Filippov, S.J. Elston. *J. Opt. A: pure appl. Opt.*, **2**, 27 (2000).

[15] T.M. Nicholson. *Mol. Crystl. Liq. Cryst.*, **177**, 163 (1989).
[16] V.K. Gupta, N.L. Abbott. *Langmuir*, **15**, 7213 (1999).
[17] K. Yee. *IEEE Trans. Antennas Propag.*, **14**, 302 (1996).
[18] A. Taflove. *Wave Motion*, **10**, 547 (1998).
[19] J.P. Berenger. *Comput. Phys.*, **114**, 185 (1994).
[20] G. Mur. *IEEE Trans. Electromagn. Compat.*, **23**, 377 (1981).
[21] P.R. Witzigmann, W. Fichtner. *J. opt. Soc. Am. A*, **15**, 753 (1998).
[22] C.M. Titus, P.J. Bos, J.R. Kelly, E.C. Gartland. *Jpn. J. appl. Phys.*, **3A**, 1488 (1999).
[23] E.E. Kriezis, S.J. Elston. *Opt. Commun.*, **165**, 99 (1999).
[24] E.E. Kriezis, C.J.P. Newton, T.P. Spiller, S.J. Elston. *Optics*, **41**, 5346 (2002).
[25] K.G. Vinay, L.A. Nicholas. *Langmuir*, **15**, 7213 (1999).
[26] A.F. Konstantinova, K.K. Konstantinov, B.V. Nabatov, E.A. Evdishchenko. *Phys. Prop. Cryst.*, **47**, 645 (2002).
[27] H. Wohler, G. Hass, M. Fritsch, D.A. Mlynski. *J. opt. Soc. Am. A*, **5**, 1554 (1988).
[28] A. Taflove. *Computational Electrodyanmics: The Finite-Difference Time- Domain Method*. Artech House, Norwood (2000).
[29] Matlab 6.5., the Mathworks, Natick (2003).
[30] D.M. Sullivan. *IEEE, Mic.Guid. Wave Lett.*, **7**, 184 (1997).
[31] D.M. Sullivan. *IEEE, Mic.Guid. Wave Lett.*, **6**, 97 (1996).
[32] J.P. Berenger. *J. comput. Phys.*, **127**, 363 (1996).
[33] T. Scharf, C. Bohley. *Mol. Cryst. liq. Cryst.*, **375**, 491 (2002).
[34] P.G. De Gennes, J. Prost. *The Physics of Liquid Crystals*. Oxford University Press, Oxford (1993).